Sensors and Materials, Vol. 38, No. 8 (2026) 4735–4758
MYU Tokyo

S & M 4591

Sensor Technologies for Worker Safety: Integration of Ultra-wideband and an Inertial Measurement Unit for Hazard Monitoring in a Water Treatment Facility

Shiau-Jing Ho,[1] Cheng-Ching Wang,[2] Jie-Ru Yang,[2]
Hui-Ping Tserng,[1] Ming-Yen Tsou,[2] and Wen-Ping Chen[2*]

[1]Department of Civil Engineering, College of Engineering, National Taiwan University,
No. 1, Sec. 4, Roosevelt Rd., Taipei 106319, Taiwan (R.O.C)
[2]Department of Electrical Engineering, National Kaohsiung University of Science and Technology,
No. 415, Jiangong Rd., Sanmin Dist., Kaohsiung City 807618, Taiwan (R.O.C)

(Received May 11, 2026; accepted July 28, 2026)

Keywords: industrial safety helmet, indoor positioning, multi-dimensional positioning, confined space

Occupational safety in confined, metal-dense environments such as water treatment plants (WTPs) requires high-precision monitoring to mitigate risks such as falls and toxic gas exposure. In this study, a sensor-driven monitoring system was designed for narrow, enclosed reverse osmosis water treatment rooms. The system tracks localized environmental parameters to prevent equipment failure and ensure operator safety in confined high-humidity zones. We developed a multi-functional safety helmet integrating ultra-wideband (UWB) for positioning, a nine-axis inertial measurement unit for kinematic analysis, and a gas-sensing network. To overcome the non-line-of-sight and multipath interference typical of industrial geometries, an extended Kalman filter was implemented to fuse UWB ranging with pedestrian dead reckoning. The test results demonstrated a battery endurance of 12.5 h, successfully operating for full work shifts. The fall detection algorithm identified distinct kinematic phases, recording an impact peak of 11.59 g. Field testing in a WTP in Taipei, Taiwan, showed that the fusion algorithm smoothed trajectories compared with erratic UWB trilateration. Environmental sensors maintained real-time monitoring of chlorine (0.07–0.09 ppm) and methane (200–300 ppm) concentrations, both well within safety thresholds. This research advances sensor technology by demonstrating a robust, multimodal architecture that ensures centimeter-level accuracy and reliable anomaly reporting in hazardous narrow-space environments where single-source sensing traditionally fails.

1. Introduction

Working conditions in confined environments, such as the reverse osmosis (RO) rooms of water treatment plants (WTPs), pose significant occupational hazards. These include slips, trips, falls, heat stress, and respiratory distress due to inadequate ventilation. In such settings,

*Corresponding author: e-mail: wpc@nkust.edu.tw
https://doi.org/10.18494/SAM6427

ISSN 0914-4935 © MYU K.K.
https://myukk.org/

traditional safety signage alone is insufficient, as workers remain vulnerable to poor visibility, slippery floors, electrical hazards, and exposure to toxic or flammable gases.[1] Therefore, real-time monitoring and proactive risk-mitigation measures are essential to prevent unexpected accidents and ensure a rapid emergency response.

For effective monitoring and risk prevention, technologies such as real-time personnel tracking, automatic fall detection, and environmental sensing have become indispensable. For indoor positioning, active radio frequency identification (RFID)-based IoT systems have been widely adopted, offering extended transmission ranges and accuracies of approximately 30 cm.[2] Recently, ultra-wideband (UWB) wireless communication has been widely used as a robust solution for centimeter-level (10–30 cm) indoor localization.[3,4] UWB performs reliably in environments with multipath interference and structural barriers, surpassing RFID,[5] Bluetooth,[6] and Wi-Fi,[7,8] in personnel tracking for confined facilities such as WTPs. Its wide bandwidth and ultra-short pulses, often under a nanosecond, deliver centimeter-level accuracy by enabling precise time of flight measurements. In confined spaces, sensor signals often reflect off metallic equipment and concrete walls, producing multipath effects. Because UWB pulses are so brief, receivers can separate a direct line-of-sight signal from delayed reflections. Such robustness against multipath errors makes UWB data more accurate in narrow industrial spaces than conventional narrowband systems such as Wi-Fi or Bluetooth.[9]

However, the conventional three-point positioning method presents geometric instability. Limitations in anchor (a fixed reference node or base station that is installed at a known location in the environment) deployment cause collinearity or elongated triangular configurations, reducing stability and accuracy. To mitigate the susceptibility of single-method indoor positioning to occlusion, multipath effects, and cumulative errors, Ali *et al.* introduced pedestrian localization using UWB signals and inertial measurement units (IMU).[10] They employed four UWB anchors and mounted a UWB tag with a MEMS-IMU on the subject's foot. Dynamic walking tests were conducted along a rectangular trajectory, with intentional human-induced occlusion to simulate non-line-of-sight (NLOS) conditions. They compared tightly coupled, loosely coupled, error-compensation, and filtering approaches to assess their impact on localization accuracy.[10] The degradation of positioning accuracy in indoor NLOS environments is caused by UWB ranging errors and pedestrian dead reckoning (PDR) drift. Using smartphone IMU data, PDR is used to enhance deep-learning-based speed estimation, replacing traditional step detection and stride length estimation. UWB positioning is further employed to correct heading errors induced by smartphone tilt. A Kalman filter was then used to fuse UWB positioning with UWB-assisted PDR, thereby improving pedestrian localization outcomes.[11] The vulnerability of low-cost UWB/IMU fusion positioning to outliers and measurement noise in complex non-Gaussian environments can be reduced by combining a robust unscented Kalman filter with maximum correntropy.[11] Such a system was validated using a low-speed autonomous ground vehicle platform equipped with UWB, IMU, global navigation satellite system, inertial navigation system, and camera/light detection and ranging sensors. The system's performance was validated on narrow campus roads under line-of-sight, semi-simulated NLOS, and non-Gaussian noise conditions, presenting improved positioning accuracy.[12]

Such results show that UWB enables absolute distance measurements in indoor settings, IMU/PDR enables short-term continuous displacement estimation, and Kalman filtering effectively fuses heterogeneous sensor data while mitigating measurement errors. However, previous studies on pedestrian localization have largely focused on algorithmic accuracy, filtering strategies, and trajectory error reduction, with limited attention to operations in indoor facilities, where anchor deployment is constrained, equipment occlusion and metallic reflections are prevalent, walkways are narrow, and workers must wear safety helmets while conducting the required real-time anomaly reporting.

Automated fall detection is another critical component of intelligent hazard prevention systems. AI-driven computer vision models, particularly the You Only Look Once (YOLO) series, have been widely utilized.(13) However, their effectiveness in confined spaces is limited owing to difficulties in camera installation and environmental interference, such as steam and low-light conditions. Environmental sensing is also vital to mitigate biochemical risks, including hypoxia, hydrogen sulfide, and chlorine exposure. Therefore, integrated gas sensing networks are required to continuously monitor hazardous parameters.(14) Recent advancements in sensor materials have expanded gas detection capabilities. For example, methane selectivity has been significantly enhanced using platinum-decorated zinc oxide nanorods on microcantilever surfaces.(15) Similarly, $MoS_2/Ce_2Sn_2O_7$ heterojunctions synthesized using hydrothermal methods have improved detection selectivity and sensitivity to ammonia and a range of volatile organic compounds at room temperature.(16) These developments highlight the increasing importance of advanced sensor technologies in industrial safety applications.

Recent smart helmets are designed mainly for fall detection or GPS tracking in open construction sites.(17,18) In this study, we designed a safety helmet that integrates UWB positioning, a nine-axis IMU for motion tracking, and a gas-sensing network for indoor work environments. The helmet reduces localization errors from weak trilateration geometry, signal blockage, and multipath interference in confined spaces, while also detecting worker falls. We introduce a dual-layer sensor system tailored for the reflective, humid conditions of WTPs. Through the integration of UWB positioning with environmental sensors, severe signal loss caused by dense metallic piping and concrete walls is prevented. The modular design can be used in other hazardous areas. Gas sensors are employed to continuously measure hazardous chemical concentrations during operations. With the features of localization, fall detection, gas monitoring, and real-time reporting combined, the system improves worker safety. The monitoring architecture addresses ventilation, humidity, and safety challenges specific to confined rooms of WTPs. Sensor placement is optimized to minimize signal attenuation in narrow, metallic-shielded spaces. We validated the performance of the safety helmet designed by measuring sensor responsiveness and signal reliability under sustained humidity typical of active filtration plants.

2. System Architecture

2.1 Hardware architecture

We implemented a safety monitoring system in a helmet for the real-time tracking of personnel in confined spaces and to provide immediate alerts for falls or hazardous gas leaks. The system comprises the helmet and a cloud management platform (Fig. 1). We chose a helmet over a wristband because of the structural and operational advantages of a helmet in WTPs. Wristbands move rapidly during manual maintenance, producing motion artifacts in sensor data. Workers also immerse their hands in water or reach into narrow metallic machinery, which weakens radio signals and exposes wrist devices to impact. The helmet offers a stable, elevated position that maintains line-of-sight with UWB anchors, reducing localization errors. Although helmet-mounted sensors could measure concentrations near the worker's breathing zone, the chemical sensors in the present system were installed at fixed monitoring stations to improve measurement stability and avoid compromising the structural integrity of the helmet.

We selected chlorine and methane for detection because these gases present the most immediate risks in enclosed RO water treatment rooms. Chlorine is widely used for biofouling control and membrane disinfection, and its leakage causes a serious hazard.[19] Methane poses a major risk of explosion and asphyxiation, as anaerobic conditions in stagnant water or drainage channels cause its rapid accumulation.[20] Although other industrial gases occur in WTPs, chlorine and methane are critical gases causing acute toxicity and posing an explosion risk in limited spaces. The modular communication interface allows operators to add further sensors if facility processes change.

We separated chemical sensors from the helmet to improve detection accuracy and maintain structural safety. Reliable monitoring of gas accumulation requires sensors placed at static, mapped points across the facility with continuous exposure. Mounting them on the helmet reduces accuracy and durability because worker movement creates turbulent airflow that distorts concentration readings. Helmet-mounted sensors also need vent openings in the outer shell of

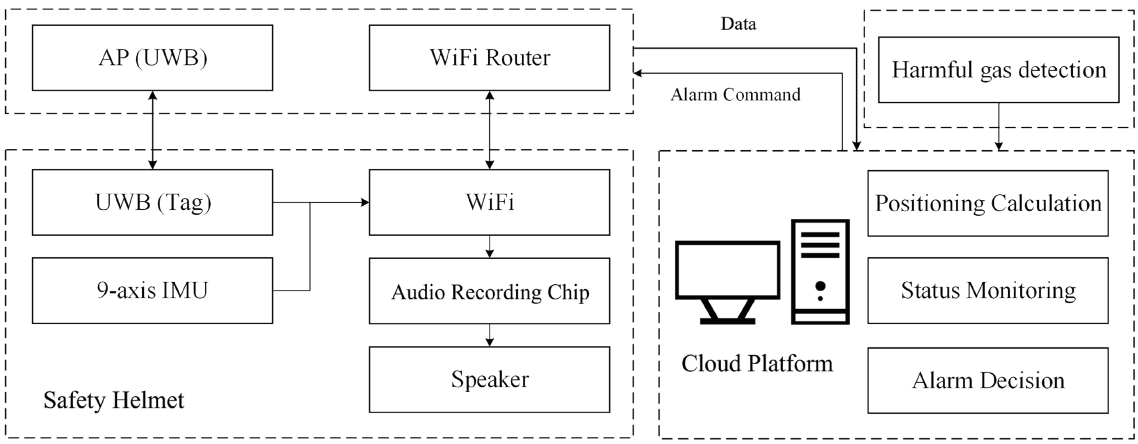

Fig. 1. Architecture of system developed for safety monitoring.

the helmet, which compromise impact resistance and violate industrial safety standards. Our design instead keeps the helmet in wireless communication with the fixed sensor network, ensuring workers receive immediate alerts about local chemical hazards without compromising the protective function of the helmet.

The safety helmet serves as the data acquisition device for personnel monitoring in confined working environments. It integrates a microcontroller unit (MCU), UWB, IMU, and Wi-Fi modules. Upon activation, the MCU captures ranging data from UWB base stations deployed in the workspace, along with motion and orientation data from the IMU. This information is transmitted through Wi-Fi to the cloud platform. The helmet incorporates an audio recording chip and speaker, enabling two-way communication. Alarm commands generated by the cloud platform can be relayed back to the worker in real time, ensuring immediate hazard notification.

The platform utilizes UWB data to calculate the user's coordinates on the basis of trilateration. However, in confined environments where spatial constraints lead to collinearity or poor geometric dilution of precision (GDOP, acute angles less than 10°), standard trilateration becomes unreliable. In this case, IMU data are used to refine the helmet's position, effectively mitigating signal interference issues inherent to confined spaces (Fig. 2). During sewage treatment, the decomposition of organic matter causes risks of flammable and explosive methane accumulation, whereas chlorine used for disinfection also presents high toxicity hazards. Monitoring these gases is vital for personnel safety.

The system integrates the safety helmet with two complementary fixed gas-sensing technologies to ensure atmospheric safety in the WTP. First, the MQ-4 sensor (Hanwei Electronics, China) was used. It is a metal oxide semiconductor device specifically designed for detecting methane and natural gas. It operates across a wide detection range of 200–10000 ppm and is highly sensitive to methane, although its readings are affected by ambient temperature and humidity. In this study, the MQ-4 is used primarily for trend monitoring, allowing relative

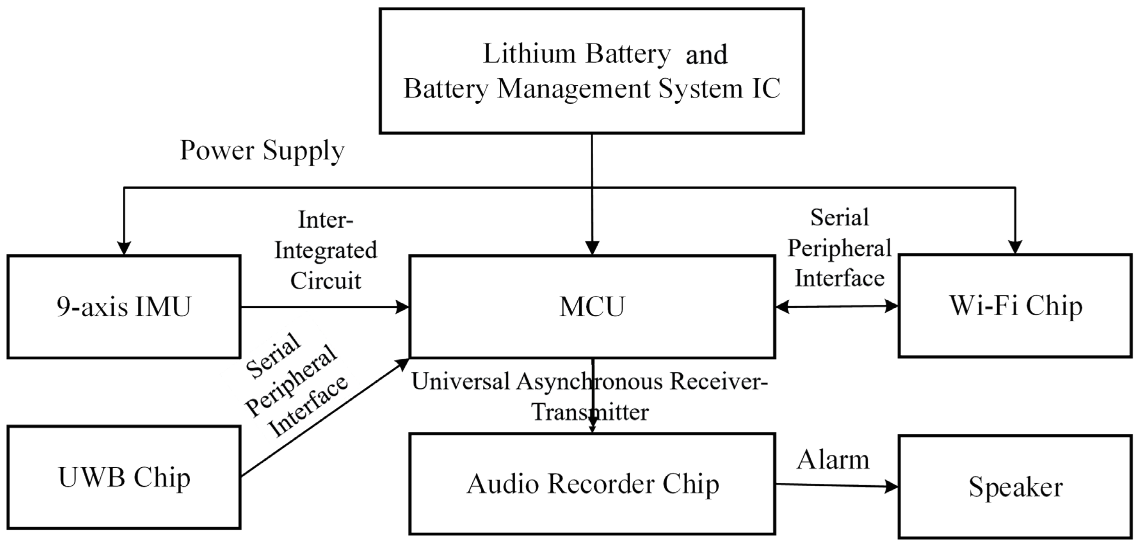

Fig. 2. Hardware architecture of safety helmet with multiple sensors.

concentration shifts to be tracked and ensuring that concentrations remain well below the 10% lower explosion limit of 5000 ppm. For chlorine detection, the ZE03-Cl2 electrochemical module was used (Winsen Electronics, China). Electrochemical modules provide superior selectivity and stability, which are essential for monitoring toxic gases in industrial environments. The ZE03-Cl2 offers a detection range of 0–10 ppm with a fine resolution of 0.01 ppm and a rapid response time of less than 30 s. Its dual output options [universal asynchronous receiver–transmitter (UART) or analog] and lifespan of at least two years make it well-suited for the continuous monitoring of chlorine concentrations in confined spaces.

The sensing unit employs an AC–DC power module to convert 110 V AC into stable 12 V DC (for the cooling fan) and 5 V DC (for the MCU and sensors). An active sampling method is adopted: the DC fan draws ambient air from the RO water treatment area into the sensing chamber (Fig. 3). This framework significantly reduces detection latency and enhances measurement stability compared with passive diffusion. For methane detection, the sensor outputs an analog voltage signal, which is digitized by the MCU's internal analog-to-digital converter. Multi-sampling averaging and low-pass filtering are applied to reduce environmental noise. For chlorine detection, an electrochemical sensing module communicates using a UART to provide high-precision digital concentration data. Thresholds are set according to the Ministry of Labor standards of Taiwan. For chlorine, the 8-h time-weighted average must be 0.5 ppm, with a short-term exposure limit of 1 ppm. For methane, the alert threshold is set at 10% of the lower explosive limit (LEL), corresponding to 5000 ppm; the methane LEL itself is approximately 50000 ppm. Exceeding these limits triggers an immediate anomaly alert

Table 1
Gas sensor specifications.

Sensor	Gas detected	Detection range	Specifications
MQ-4	Methane/natural gas	200–10000 ppm	Metal oxide semiconductor sensor; micro-Al_2O_3 ceramic tube with SnO_2-sensitive layer; affected by temperature and humidity
ZE03-Cl2	Chlorine	0–10 ppm	Electrochemical module; resolution, 0.01 ppm; response time, ≤30 s; UART or analog output; lifespan, ≥2 years

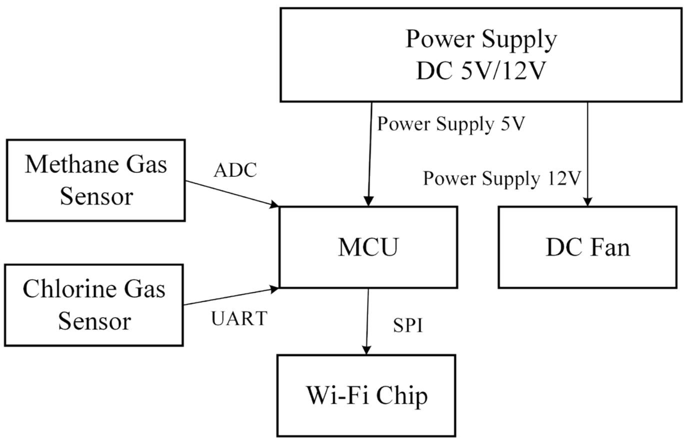

Fig. 3. Architecture of gas sensing.

transmitted via Wi-Fi to the cloud platform. The specifications of the methane and chlorine gas sensors used in this study are summarized in Table 1.

The cloud platform functions as the central hub for data collection, integrating positioning, posture, and gas concentration measurements, while also providing visualization and emergency response services. Its architecture is organized into four layers (Fig. 4). The physical sensing layer comprises the safety helmets, UWB base stations, gas sensing stations, and on-site warning devices such as LED displays and buzzers. At the gateway and messaging layer, local wireless networks and a message queuing telemetry transport (MQTT) are used to manage data traffic, including device heartbeat signals and environmental telemetry. Within the cloud application layer, positioning data are processed by a UWB positioning algorithm, whereas gas concentration data are analyzed by a diagnostic service. All processed results are securely stored in a cloud database with strict user authentication and audit logging protocols. The user layer provides a web-based dashboard that enables real-time tracking on electronic maps, playback of historical trajectories, and geofencing functions. Mobile push notifications ensure that safety supervisors receive immediate alerts during emergencies.

The system continuously operates in a closed loop. The safety helmet transmits localization and motion data, while the on-site environmental gas sensing module transmits chlorine and methane concentration data to the cloud platform. In data processing, the cloud platform calculates worker coordinates, evaluates risks, and compares sensor readings against predefined safety thresholds. Downstream, if anomalies are detected, alarm commands are transmitted through the Wi-Fi infrastructure to the helmet's speaker, ensuring that workers are promptly notified of hazards in real time.

2.2 Software architecture

2.2.1 Personnel positioning

In confined and narrow indoor environments, UWB technology is employed owing to its superior ranging accuracy and its resilience against interference compared with Wi-Fi or

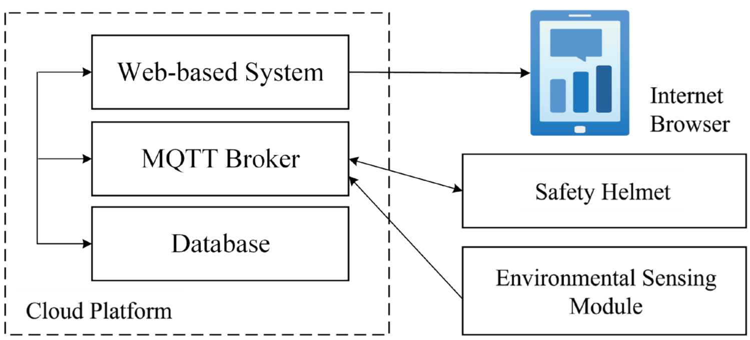

Fig. 4. (Color online) Cloud system architecture.

Bluetooth, making it well-suited for distance measurements in indoor localization. However, in WTPs, the presence of metal infrastructure, pipelines, and high-humidity conditions induces multipath interference, NLOS propagation, and signal shadowing, which can lead to transient instability or amplified errors in UWB data (Fig. 5). UWB signals propagate along direct and reflected paths. In environments with metallic surfaces or equipment, reflected signals can arrive at the receiver with varying delays, creating multipath interference that distorts distance estimation.(17) Furthermore, when physical obstructions block the direct line-of-sight path, the receiver captures attenuated or delayed signals, resulting in significant localization errors.(21) These phenomena are pronounced in geometrically constrained spaces such as RO water treatment rooms, where narrow corridors and dense infrastructure exacerbate collinearity and poor GDOP. Consequently, whereas UWB offers high accuracy in open indoor environments, its performance in confined industrial settings requires complementary sensing strategies, such as IMU fusion, to mitigate interference and ensure reliable positioning.(22)

Furthermore, spatial constraints often lead to suboptimal fixed reference points such as base stations or access points (APs) and deployment such as uneven distributions, near-collinear arrangements, or elongated triangular geometries (Fig. 6). These configurations weaken the geometric constraints between APs: (1) uneven access point distribution reduces coverage uniformity, (2) near-collinear access point placement leads to poor GDOP, and (3) elongated triangular geometries create sharp angles that amplify localization errors. Under such conditions, trilateration solutions exhibit jumping coordinates or instability, particularly in confined industrial environments. To mitigate these effects, we employed multi-sensor fusion localization, combining UWB, IMU, and PDR data, thereby enhancing robustness and accuracy in challenging deployment scenarios.

The safety helmet's MCU aggregates UWB ranging data and IMU motion data. As shown in Fig. 7, three UWB APs (AP1–AP3) provide distance measurements (d_1, d_2, and d_3) to the

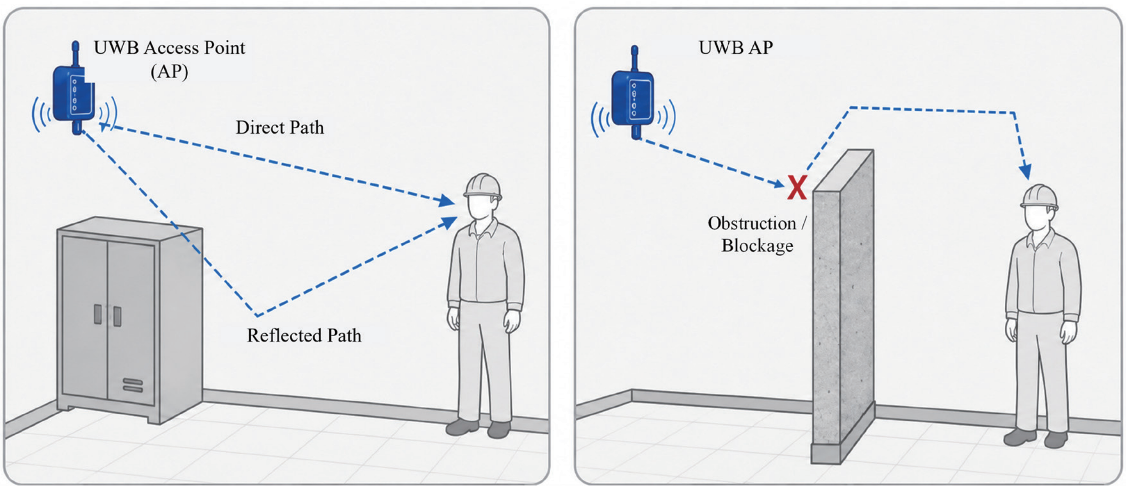

(a) (b)

Fig. 5. (Color online) UWB signal propagation and interference in confined environments. (a) Multi-path effect and (b) NLOS propagation.

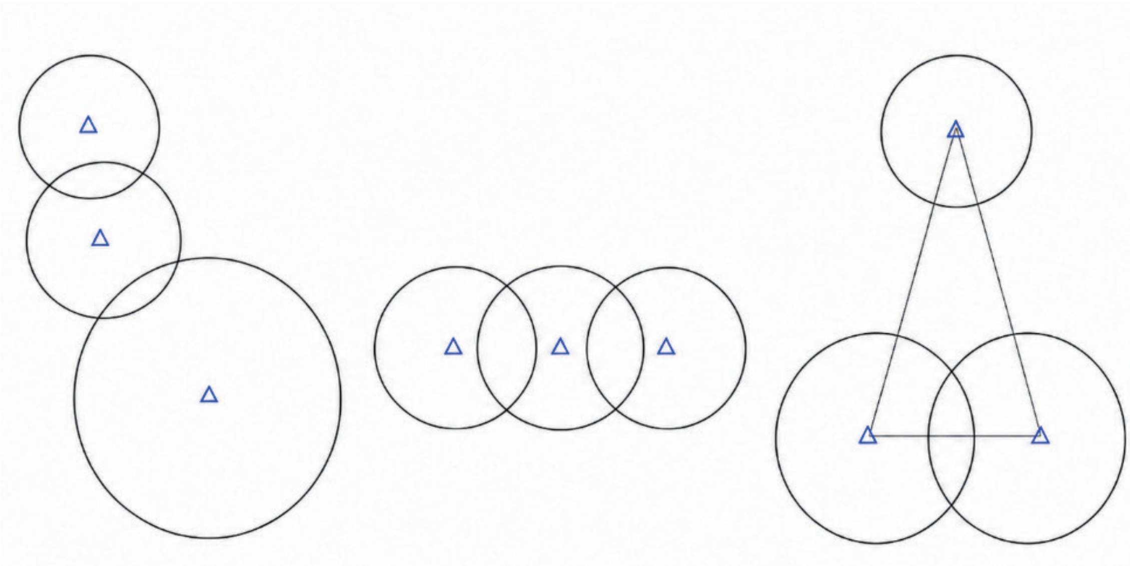

Fig. 6. (Color online) Geometrically unfavorable anchor distributions in confined environments: (a) uneven access point distribution, (b) near-collinear arrangement of three APs, and (c) elongated triangular geometry.

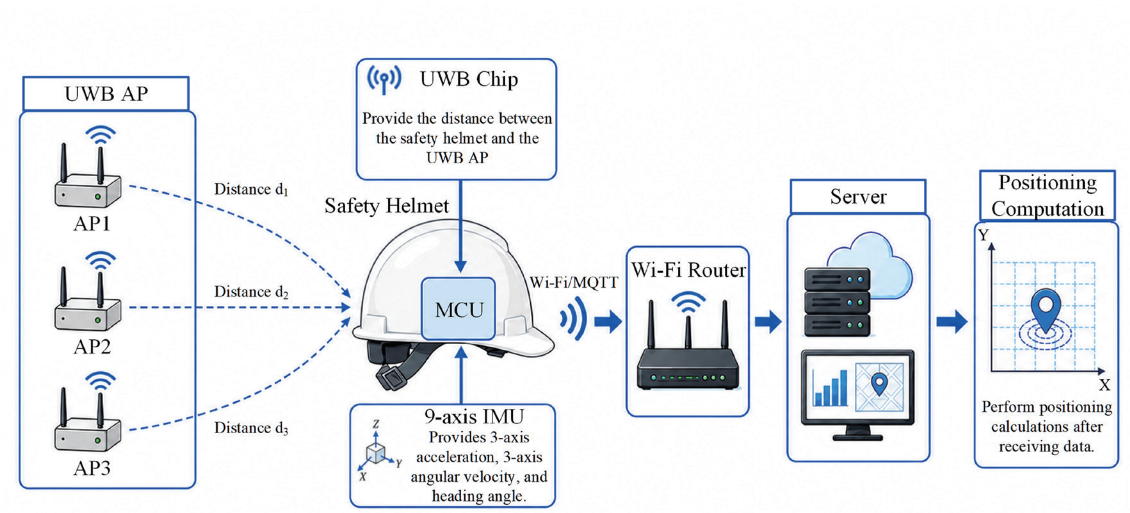

Fig. 7. (Color online) Simplified diagram of data transmission in safety helmet positioning system.

helmet's UWB chip, whereas IMU supplies three-axis acceleration, three-axis angular velocity, and heading angle information. The MCU aggregates these inputs and transmits them via Wi-Fi/MQTT to the backend server, where the sensor-fusion and positioning calculations are performed. On the server side, standard trilateration is performed when at least three APs are available. However, in situations where access point availability is poor, or GDOP is high, the system leverages IMU-based PDR to estimate short-term displacement, thereby stabilizing localization accuracy. All sensor data are encapsulated into JavaScript Object Notation format and transmitted through MQTT on the Wi-Fi network for fused calculation. The server computes the helmet's position on an *X*–*Y* coordinate system, enabling continuous real-time tracking of personnel within confined environments.

2.2.2 Extended Kalman filter (EKF) fusion

The system employs an EKF to fuse UWB distance data with IMU and PDR displacement predictions. EKF is used for prediction and update. PDR data are used to provide continuous relative motion estimates, whereas UWB ranging data are used to identify absolute distance constraints that correct the cumulative drift inherent in PDR.

A two-dimensional Cartesian coordinate system is established, with APs fixed at known positions. Initialization requires defining the state vector and covariance matrices. The EKF state vector at time k is defined as

$$x_k = \begin{bmatrix} x_k \\ y_k \end{bmatrix}, \tag{1}$$

where x_k and y_k denote the helmet's 2D coordinates in the coordinate system.

In IMU and PDR displacement prediction, the PDR branch uses three-axis acceleration to detect step events and heading angles to estimate movement direction. When a step of length L is detected at time k with heading angle θ, the predicted position is determined as follows.

$$\begin{cases} \hat{x}_{k|k-1} = \hat{x}_{k-1} + L \cdot \cos(\theta) \\ \hat{y}_{k|k-1} = \hat{y}_{k-1} + L \cdot \sin(\theta) \end{cases} \tag{2}$$

Here, $\hat{x}_{k|k-1}$ and $\hat{y}_{k|k-1}$ are the predicted coordinates before the EKF update. The general state is predicted as

$$\hat{x}_{k|k-1} = f\left(\hat{x}_{k-1}, u_k\right) + w_k\,, \tag{3}$$

where u_k is the IMU/PDR input and w_k is system noise. The predicted error covariance $P_{k|k-1}$ is updated as

$$P_{k|k-1} = F_k P_{k-1} F_k^T + Q\,, \tag{4}$$

where F_k is the Jacobian of the state transition function. Since PDR inputs are added to the previous state, F_k is approximated as the identity matrix ($F_k \approx I$).

For the i-th UWB access point located at (x_i,y_i), the Euclidean distance to the helmet at (x,y) is calculated as

$$d_i = \sqrt{\left(x - x_i\right)^2 + \left(y - y_i\right)^2} \,. \tag{5}$$

$\hat{y}_{k|k-1}$

The theoretical distance $h_i\left(\hat{x}_{k|k-1}\right)$ is estimated on the basis of the predicted state.

$$h_i\left(\hat{x}_{k|k-1}\right) = \sqrt{\left(\hat{x}_{k|k-1} - x_i\right)^2 + \left(y_{k|k-1} - y_i\right)^2} \tag{6}$$

The actual UWB observation $z_{i,k}$ is then defined as

$$z_{i,k} = d_{i,k} + v_{i,k} \,, \tag{7}$$

where $v_{i,k}$ is the observation noise. For n APs, the observation vector Z_k and the function matrix $h\left(\hat{x}_{k|k-1}\right)$ are defined as

$$z_k = \begin{bmatrix} z_{1,k} \\ \vdots \\ z_{n,k} \end{bmatrix}, \quad h\left(\hat{x}_{k|k-1}\right) = \begin{bmatrix} h_1\left(\hat{x}_{k|k-1}\right) \\ \vdots \\ h_n\left(\hat{x}_{k|k-1}\right) \end{bmatrix}. \tag{8}$$

To prevent NLOS or multipath errors from causing coordinate jumps, the system calculates the residual between the actual and theoretical distances (v_k, innovation).

$$v_k = z_k - h\left(\hat{x}_{k|k-1}\right) \tag{9}$$

The innovation covariance S_k is calculated as

$$S_k = H_k P_{k|k-1} H_k^T + R \,, \tag{10}$$

where H_k is the Jacobian of the observation functi$\hat{y}_{k|k-1}$he observation function of each access point is defined as

$\hat{x}_{k|k-1}$

$$H_i = \begin{bmatrix} \dfrac{\hat{x}_{k|k-1} - x_i}{h_i\left(\hat{x}_{k|k-1}\right)} & \dfrac{y_{k|k-1} - y_i}{h_i\left(x_{k|k-1}\right)} \end{bmatrix}. \tag{11}$$

An anomaly detection threshold γ is applied as

$$v_k^T S_k^{-1} v_k > \gamma \,. \tag{12}$$

If this condition holds, the UWB measurement becomes suspicious. The system then increases the corresponding R value to reduce trust in that access point or excludes it from the update. Finally, the Kalman gain K_k, the fused state $\hat{x}_k$, and the error covariance P_k are computed as follows.

$$K_k = \hat{x}_{k|k-1_1} H_k^T S_k^{-1} \tag{13}$$

$$\hat{x}_k = x_{k|k-1} + K_k v_k \tag{14}$$

$$P_k = \left(I - K_k H_k\right) P_{k|k-1} \tag{15}$$

The overall workflow of EKF fusion is shown in Fig. 8.

2.2.3 Fall detection

The fall detection algorithm is created on the basis of the analysis of tri-axial acceleration and angular velocity signals captured by the IMU. A typical fall event consists of three kinematic phases.

- Free-fall phase: During the initial descent, the resultant acceleration magnitude drops significantly below the standard gravitational acceleration (1 g) owing to the transient weightless state induced by downward motion.
- Impact phase: Upon contact with the ground or surrounding infrastructure, both the accelerometer and gyroscope record sharp, high-magnitude spikes in signal intensity.
- Stationary phase: Following impact, the individual typically remains immobile owing to injury or shock. In this state, the acceleration magnitude stabilizes near 1 g, and angular velocity fluctuations diminish to baseline levels.

To identify these phases within a continuous time window, the signal vector magnitude is calculated for acceleration and angular velocity, ensuring orientation-independent detection. The

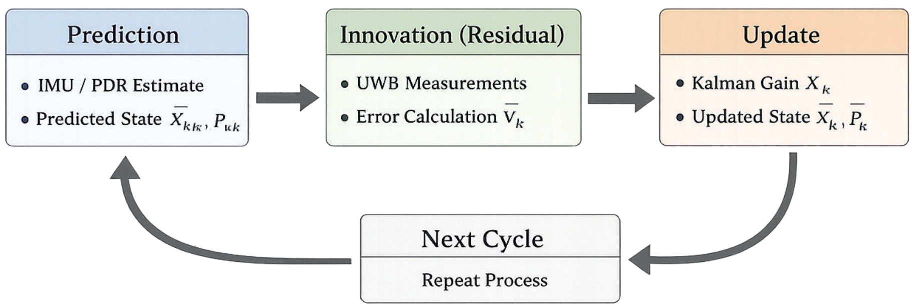

Fig. 8. (Color online) Workflow of the EKF-based UWB/IMU/PDR fusion algorithm developed in this study.

tri-axial resultant acceleration magnitude is defined as

$$A_{total,t} = \sqrt{a_{x,t}^2 + a_{y,t}^2 + a_{z,t}^2} \ . \tag{16}$$

Here, $A_{total,t}$ represents the total acceleration magnitude at time t, derived from the instantaneous acceleration components $a_{x,t}$, $a_{y,t}$, and $a_{z,t}$ along the IMU's three axes. The tri-axial resultant angular velocity magnitude is expressed as

$$G_{total,t} = \sqrt{\omega_{x,t}^2 + \omega_{y,t}^2 + \omega_{z,t}^2} \ , \tag{17}$$

where $G_{total,t}$ denotes the total angular velocity magnitude at time t, computed from the instantaneous angular velocities $\omega_{x,t}$, $\omega_{y,t}$, and $\omega_{z,t}$ along the IMU's axes. Including G_{total} is critical for distinguishing genuine falls, which involve rapid postural rotation or violent shaking, from simple linear vibrations, thereby reducing false positives. The fall detection framework employs a sequential three-step verification process within a sliding time window.

- Free-fall detection: The system identifies a free-fall event when Atotal falls below 0.3 g for more than 100 ms, indicating a transient loss of support.
- Impact identification: Following a detected free-fall event, the subsequent 500-ms window is examined for an impact peak in Atotal exceeding 3.0 g, together with a marked increase in angular velocity.
- Post-fall stability check: The system verifies whether the user has entered a stationary state, characterized by $A_{total} \approx 1\ g$ and minimal angular velocity variance.

If all three conditions occur sequentially, the system triggers a fall event alarm. The associated metadata, including event timestamp, device ID, peak acceleration and angular velocity values, and incident classification, is transmitted to the backend server using the MQTT protocol. The monitoring interface generates an instantaneous emergency alert to facilitate rapid intervention.

3. Results

3.1 Safety helmet fabrication

A prototype of the multi-functional safety helmet developed in this study is shown in Fig. 9. The helmet integrates a UWB positioning module for high-precision ranging, IMU for kinematic state estimation, and an audio module for real-time safety alerts. The core control unit is an ESP32-S3-WROOM-1 MCU, which manages data acquisition from these heterogeneous sensors and facilitates wireless transmission on the basis of the MQTT protocol.

Figure 10 shows the battery discharge characteristics of the safety helmet during a continuous operation test where UWB, IMU, Wi-Fi, and MQTT functions were simultaneously active. The initial voltage of approximately 4.05 V exhibited a linear decay over time. After 12.5 h of continuous operation, the voltage reached the critical shutdown threshold of 3.3 V. This

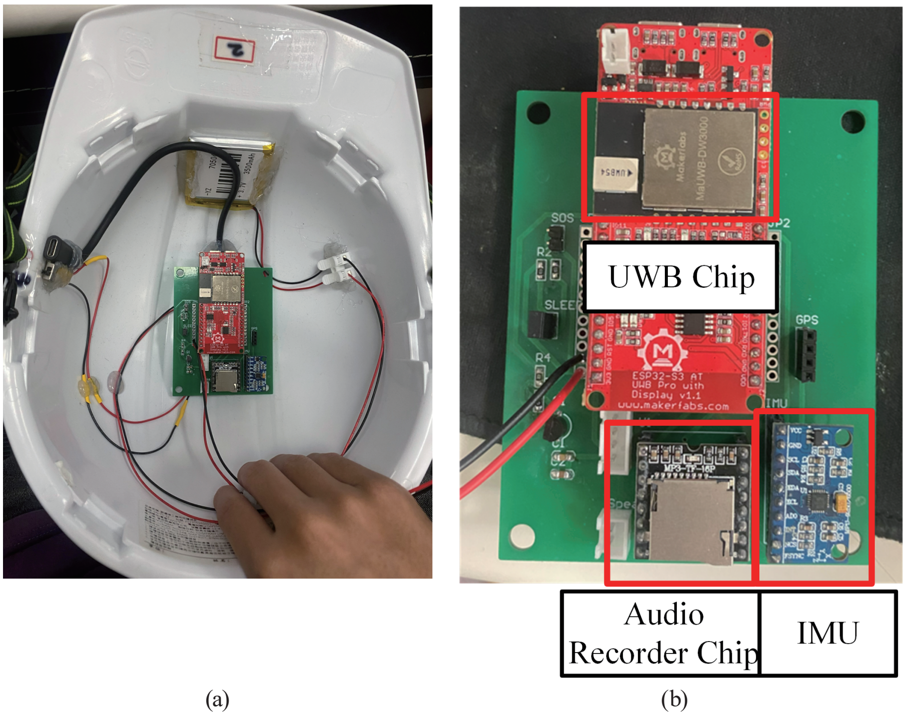

Fig. 9. (Color online) (a) Prototype safety helmet and (b) its components.

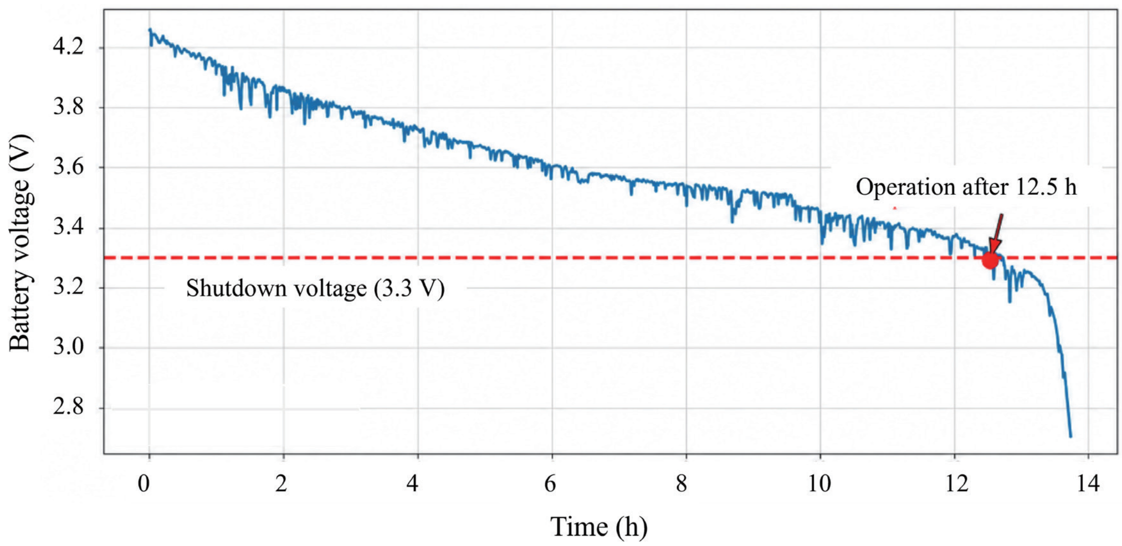

Fig. 10. (Color online) Battery voltage discharge curve under full operational load with UWB, IMU, and Wi-Fi active.

endurance exceeds the standard 8-h work shift requirement, confirming the system's operational viability for full-day industrial monitoring without requiring mid-shift recharging.

3.2 Fall detection and data transmission

The system utilizes a structured data format for seamless integration with the backend server, as shown in the JSON payloads. The UWB packet provides millisecond-precise timestamps and multi-access point ranging data (cm), whereas the IMU packet encapsulates tri-axial motion data and a Boolean fall flag. The fall detection performance was validated through controlled incident simulations. As shown in Fig. 11, the free-fall phase is characterized by a pronounced drop in acceleration magnitude below the gravitational baseline, confirming the transient loss of support. The subsequent impact phase produces a sharp acceleration spike, reaching 11.59 *g* in the test, corresponding to the moment of collision with the ground. Immediately afterward, the signal stabilizes near 1 *g*, marking the post-impact stationary phase, during which the acceleration magnitude remains close to 1 *g* and the angular motion is minimal. The transmitted payload includes the peak acceleration and peak angular velocity, offering a quantitative measure of impact severity for emergency responders. The message also contains the device ID and timestamp, enabling precise event correlation with spatial data from UWB. This multi-stage verification through the combination of temporal, kinematic, and network-level evidence significantly reduces false positives in dynamic industrial environments,(17) ensuring that genuine fall events trigger alerts and intervention protocols.

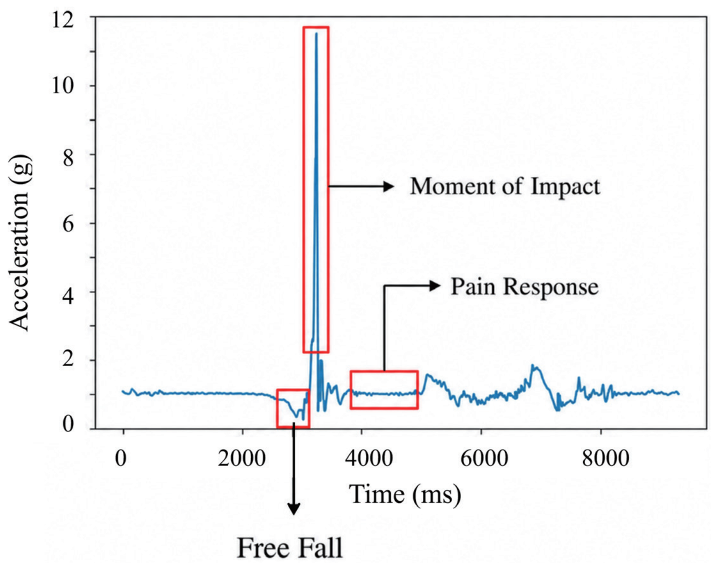

Fig. 11. (Color online) Acceleration magnitude profile in fall detection.

3.3 Environmental gas monitoring

The environmental sensing unit was deployed within the RO water treatment area of a WTP in Taipei, Taiwan (Fig. 12). Encased in a durable, chemically resistant acrylic housing, the unit continuously monitors methane and chlorine concentrations. Gas monitoring units were strategically installed on major pipelines and machinery to ensure representative sampling of the ambient environment.

Chlorine concentrations fluctuated between 0.07 and 0.09 ppm during the monitoring period. These values are below the 0.5 ppm permissible exposure limit defined by the Ministry of Labor of Taiwan, confirming a safe working environment for personnel. Methane concentrations ranged between 200 and 300 ppm. Although the MQ-4 sensor was used for semi-quantitative trend monitoring owing to its sensitivity, the results demonstrated that methane concentrations remain far below the alarm threshold of 5000 ppm, corresponding to 10% of the methane LEL. The readings remained far below the 5000-ppm alarm threshold, corresponding to 10% of the methane LEL. However, because the MQ-4 sensor was used for semiquantitative trend monitoring, these readings should not be interpreted as certified safety measurements (Fig. 13). All sensor data were transmitted to a cloud platform for long-term historical analysis and compliance tracking. This enables proactive occupational health and safety management, ensuring that both chlorine and methane concentrations remain below safe thresholds and that deviations can be detected early.

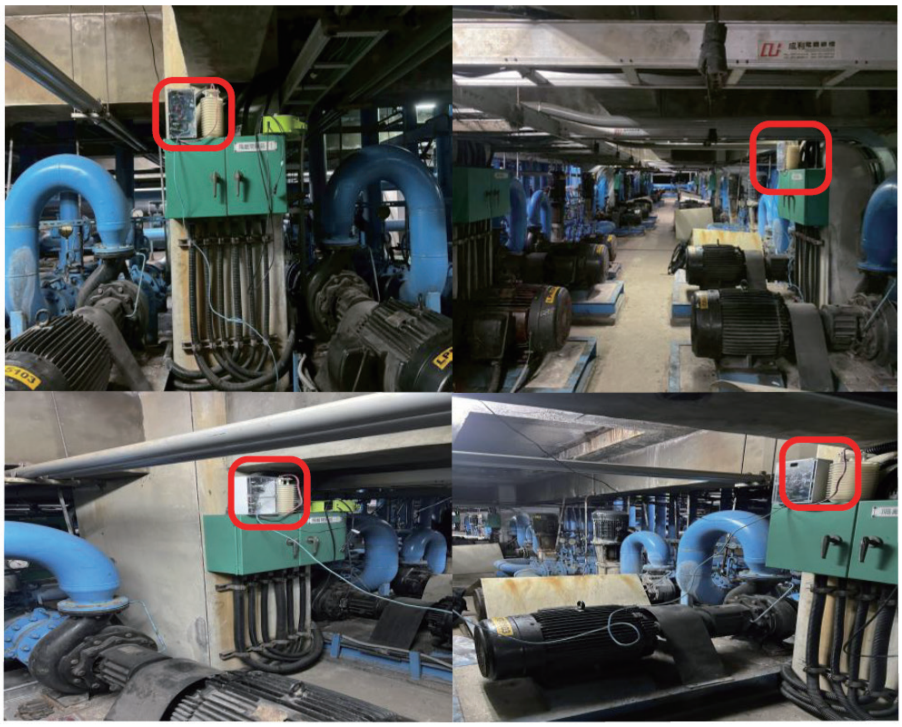

Fig. 12. (Color online) Deployment of gas monitoring units (red boxes) in WTP.

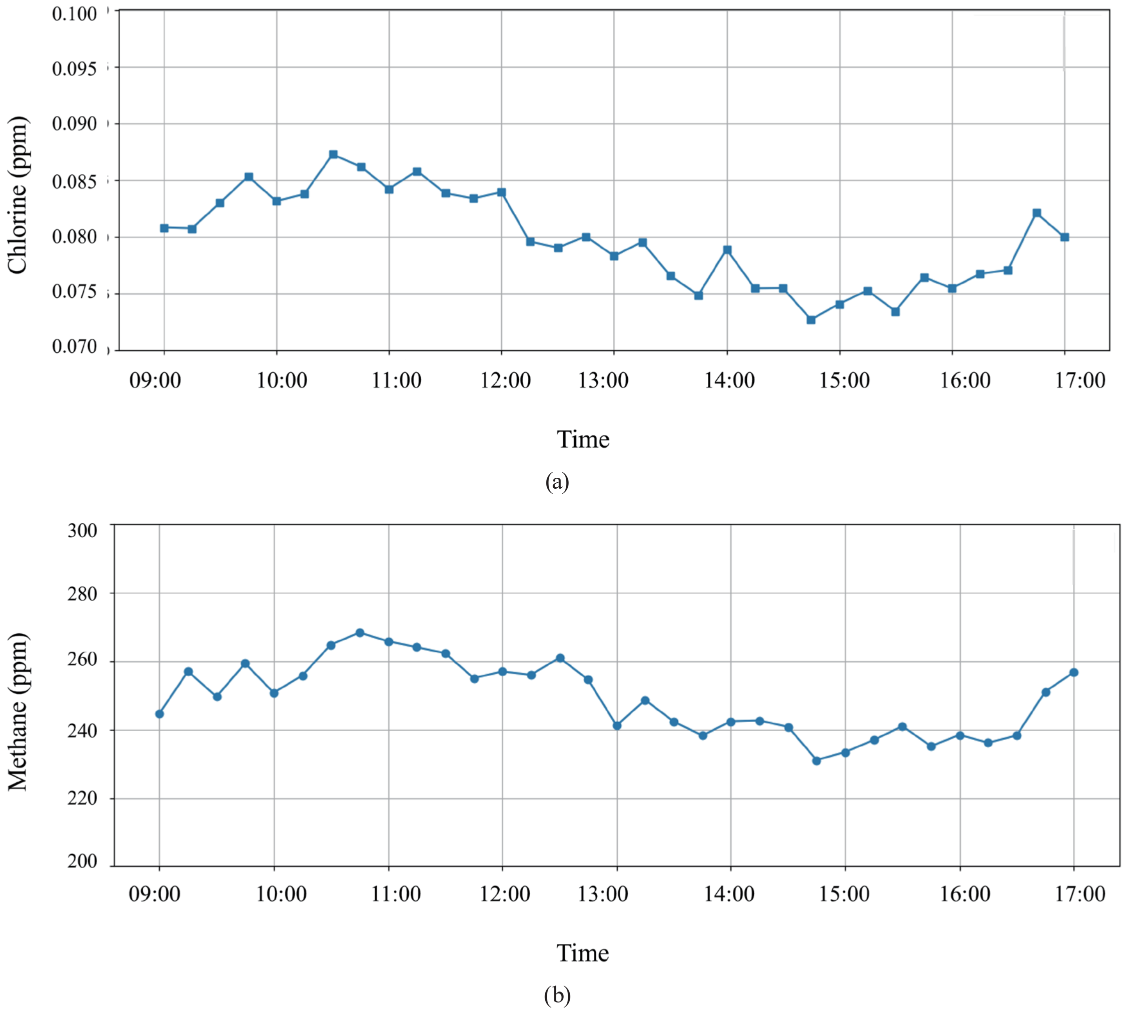

Fig. 13. (Color online) 24-h monitored environmental gas concentrations: (a) chlorine and (b) methane.

Because the field test took place in an operational municipal WTP, strict safety protocols kept ambient gas concentrations well below regulatory thresholds. As a result, sensors were not tested in acute, high-concentration leak situations. To confirm reliability under hazardous conditions without compromising facility safety, the sensors must be tested in simulated abnormal environments, such as a specialized laboratory gas chamber.(23) This controlled setting will allow the safe introduction of high-ppm chlorine and methane, enabling precise measurements of sensor response times, calibration curves under saturation, and verification of automated worker alerts during acute leak events.

3.4 Field test

We conducted a field test in the RO water treatment area of a WPT in Taipei to evaluate the localization algorithms under realistic constraints, including dense metal piping, high humidity, and complex NLOS conditions (Fig. 14). The arrangement of RO equipment created narrow

(a) (b)

Fig. 14. (Color online) Test environment: (a) dense RO equipment and (b) leaked water on floor.

corridors and obstructed sightlines, while water leakage on the floor added variability and simulated hazards workers may encounter. These conditions produced typical scenarios where multipath reflections, signal attenuation, and physical barriers degrade localization accuracy. Testing in this environment allowed us to assess the fusion algorithm under operational constraints rather than controlled laboratory settings.

The performance of the safety helmet was evaluated with three subjects, each completing five trials for a total of 15 runs. In each trial, subjects followed a standardized 50-m maintenance path inside the RO water treatment room of the WTP. Across the trials, more than 15000 spatial and environmental data points were collected, enabling repeated performance evaluation across different subjects and walking patterns.[24] The system maintained stable positioning with a mean root-mean-square error of 0.12 m across all trials, showing that worker movement and physical variation did not reduce UWB accuracy or sensor reliability. Standard fall detection systems usually place sensors on the waist or wrist, but these positions often trigger false alarms in industrial settings because of routine manual tasks.

Sensors in the helmet tolerate rapid, intentional rotations, such as checking overhead piping, without false alarms, detecting the sudden vertical acceleration drops and high-gravity impacts that mark a real slip or fall. We validated the fall detection algorithm through controlled laboratory experiments using an instrumented dummy with standard human height and weight. The helmet-mounted IMU recorded three-axis acceleration and angular velocity at 100 Hz. We simulated four fall types, forward, backward, lateral, and vertical slumps (syncope), onto a

10-cm high-density foam safety mattress.[25] In the algorithm, free fall is defined as a state when the total acceleration dropped below 0.3 *g* for more than 100 ms, followed by an impact peak above 3.0 *g* within 500 ms. To test robustness, we ran control trials where subjects performed everyday tasks such as rapid head shaking, ladder climbing, and valve inspection. The system recorded zero false positives across these activities, confirming reliable discrimination between routine movements and actual falls.

UWB APs were deployed according to the spatial constraints of the facility (Fig. 15). Because of the dense arrangement of RO equipment and obstructed sightlines, an ideal geometric distribution of APs was not achievable, which increased the GDOP. The test subject, equipped with the prototype helmet, traversed a predefined path around the equipment blocks, as shown in Fig. 16. This trajectory was intentionally designed to pass through areas with severe multipath reflections and partial occlusions, thereby simulating the operational challenges of narrow industrial spaces.

The performance of pure trilateration versus the proposed EKF-based UWB/IMU/PDR fusion algorithm is compared in Fig.17. The reconstructed trajectory exhibits significant jumping and erratic deviations. Multipath reflections from metallic surfaces and signal attenuation from high-pressure vessels introduced ranging errors, resulting in estimated positions that unrealistically intersect solid equipment or walls. This highlights the vulnerability of single-source localization in complex industrial environments. The fused algorithm's trajectory is smoother and more continuous, closely following the tester's actual path. With PDR incorporated as the process model, the system maintains a logical heading even when UWB signals are transiently unstable. The correction mechanism within the EKF effectively down-weighted erroneous UWB observations, preventing spurious jumps and ensuring trajectory consistency.

The results demonstrate that sensor fusion is critical for reliable personnel tracking in narrow-space industrial environments where single-source positioning often fails because of

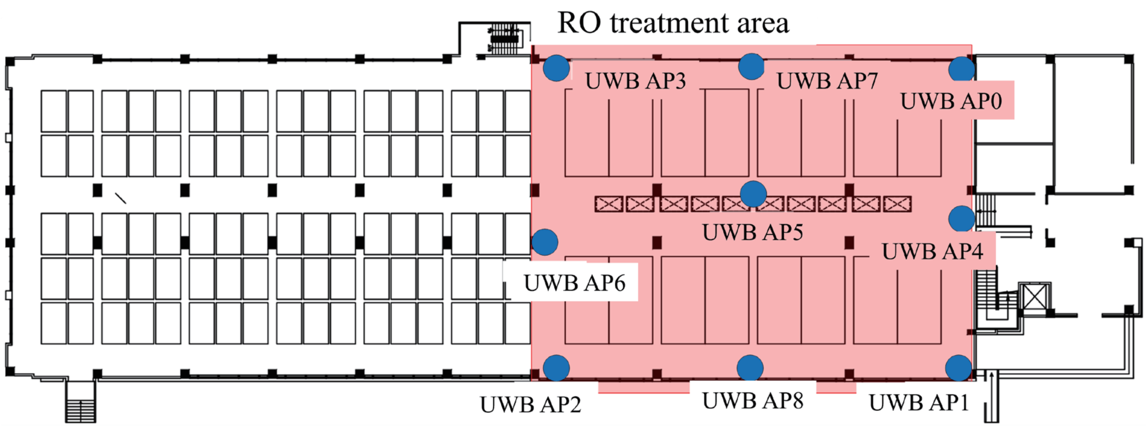

Fig. 15. (Color online) Floor plan and UWB access point deployment in RO water treatment area.

(a)

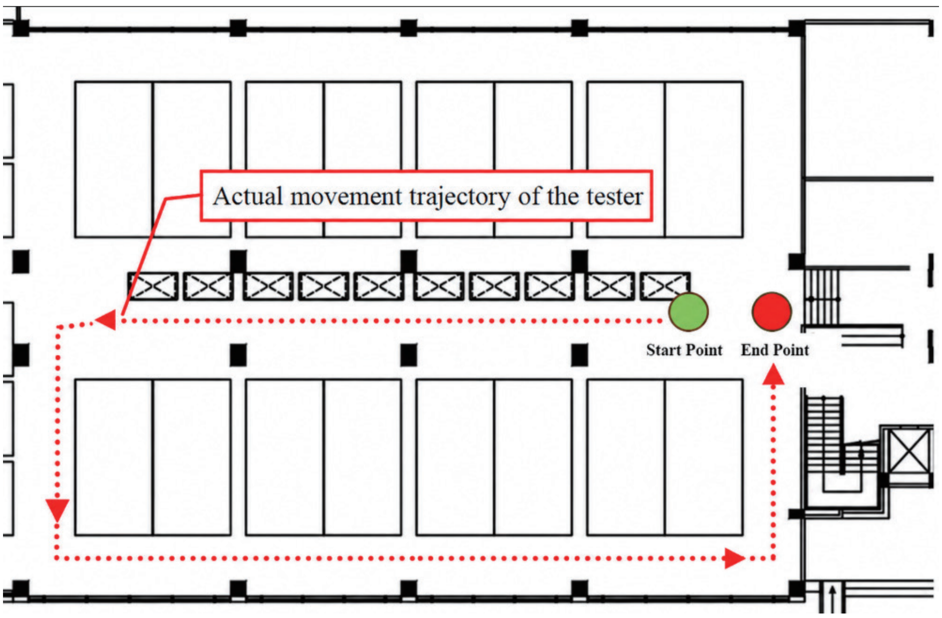

(b)

Fig. 16. (Color online) Field test procedure: (a) tester equipped with prototype and (b) predefined experimental trajectory.

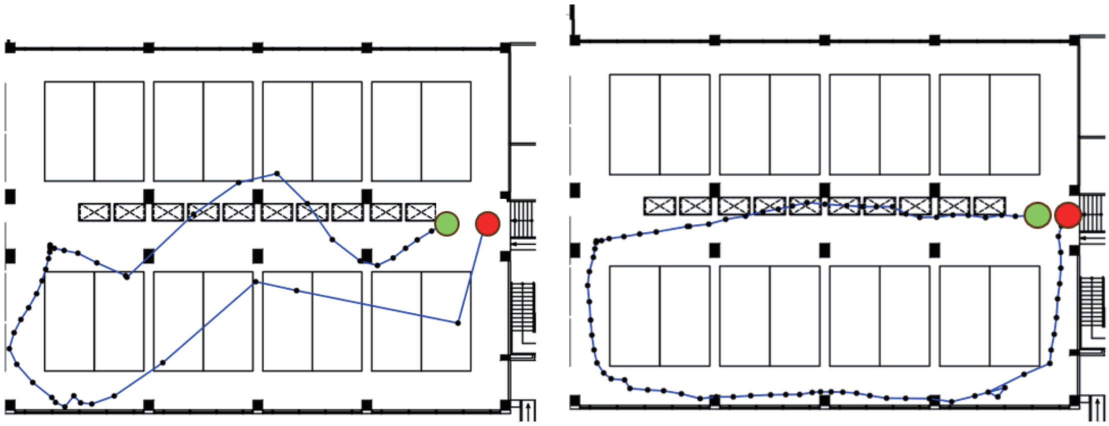

(a) (b)

Fig. 17. (Color online) Localization trajectory comparison: (a) UWB trilateration and (b) UWB/IMU/PDR EKF fusion algorithm (this study).

effects, multipath errors, and NLOS conditions, enabling continuous and realistic trajectory reconstruction that is essential for worker safety monitoring.

4. Discussion

The integration of UWB and IMU into a wearable safety helmet transforms single-source monitoring toward a robust multimodal sensor fusion architecture. RFID, Bluetooth Low Energy (BLE), and Wi-Fi round-trip time have been widely adopted for real-time localization systems, but these technologies suffer from insufficient accuracy or high susceptibility to signal attenuation in metal-dense environments.(8) In contrast, the high temporal resolution of UWB pulses enables centimeter-level ranging. In addition to UWB, the introduction of EKF relates absolute UWB positioning results to relative PDR. In complex industrial areas such as water treatment RO zones, metal infrastructure induces severe multipath interference and NLOS conditions.(26) The system effectively mitigates the coordinate jumping of pure trilateration by utilizing IMU data to provide short-term trajectory continuity.(26)

Beyond localization, the developed safety helmet in this study enables kinematic event detection. Traditional fall detection systems rely on camera-based approaches such as YOLO,(27) but these are limited by field-of-view constraints and lighting conditions in narrow industrial spaces. By employing a three-phase IMU-based detection algorithm that comprises free fall, impact, and stationary phases, we developed a system that offers a portable, privacy-preserving alternative that remains functional regardless of visual obstructions.(28) At the same time, the simultaneous monitoring of toxic gases such as chlorine and flammable gases such as methane addresses physical accidents and environmental hazards.(29) The use of electrochemical ZE03 sensors ensures high selectivity for chlorine, which is vital for preventing acute poisoning in WTPs. This integration of environmental awareness with personal kinematics significantly enhances the overall safety envelope for workers operating in high-risk zones.

Despite the performance gains demonstrated in this study, several limitations remain. The MQ-4 methane sensor, being a metal oxide semiconductor type, is cost-effective but sensitive to temperature and humidity fluctuations. It is necessary to explore advanced sensing technologies such as platinum-decorated ZnO nanorods or novel heterojunction sensors to improve selectivity and absolute accuracy at room temperature.(16) Another limitation lies in infrastructure dependency, as the system requires a pre-installed network of UWB APs. In disaster recovery scenarios or rapidly changing construction sites, anchorless or distributed time division multiple access-based localization methods provide resilience.(4) Power consumption also presents a challenge. Although the system supports a 12.5-h operation window, sufficient for a standard shift, the continuous demand for Wi-Fi and UWB transmission remains a constraint. Therefore, it is required to investigate low-power sleep modes or energy-efficient transmission protocols to extend battery life. Although the IMU-based approach reduces errors compared with pure acceleration-based methods, high-intensity work activities such as jumping or rapid tool use still might trigger false fall alarms. Incorporating machine learning at the edge to classify specific work-related motions can further refine detection accuracy and reduce false positives.(17)

In the following studies, microsensor technologies can be integrated without adding weight or power demand. Solid-state electrochemical multi-gas sensors can be used to detect a broader range of airborne toxins, including sulfur dioxide and hydrogen sulfide, maintaining a compact footprint.(30) Miniaturized photoionization detectors need to be adopted to provide real-time monitoring of trace volatile organic compounds that conventional chemical sensors miss. Flexible sweat sensors or non-invasive microneedle arrays embedded in the helmet's forehead lining can be used to monitor health indicators such as lactic acid, glucose, and electrolyte concentrations.(31) With these sensors and monitoring biomarkers, fatigue, dehydration, and heat stress can be detected, transforming the helmet from an environmental alarm into a proactive occupational health platform.

5. Conclusions

A safety monitoring system was designed for confined industrial space operation. By employing a multimodal sensor fusion architecture, we developed a system that addresses the challenges of operations in WTPs, where high humidity, narrow corridors, dense equipment layouts, and restricted visibility create hazardous working conditions. A safety monitoring and anomaly reporting system was developed around a multi-sensor safety helmet that integrates UWB positioning modules, IMU inertial sensing units, Wi-Fi/MQTT communication, a backend server, a frontend monitoring interface, and environmental gas sensors. Together, these components enable real-time tracking of worker location, movement status, and environmental safety information, thereby enhancing personnel protection during critical maintenance tasks.

The integration of UWB and IMU sensors using EKF addresses challenges in indoor positioning. Whereas UWB provides high temporal resolution for centimeter-level ranging, its vulnerability to multipath reflections and NLOS conditions in metal-dense RO water treatment zones often leads to coordinate jumping. With absolute UWB data fused with relative PDR measurements, the system ensures trajectory continuity and stability, even when physical obstructions block line-of-sight signals. Field test results confirmed that APs could not be deployed in ideal geometric positions owing to equipment density, yet the EKF-based fusion method produced smoother and more realistic trajectories than pure trilateration, demonstrating its feasibility for confined industrial environments.

The system's reliability was validated through field testing and hardware evaluation. Operational endurance tests showed linear battery endurance of 12.5 h, ensuring viability for a standard work shift. Fall detection precision was achieved through a three-phase IMU-based algorithm that successfully distinguished genuine falls from linear vibrations, recording an impact magnitude of 11.59 g and identifying post-fall stationary phases to trigger emergency notifications through MQTT. Environmental monitoring confirmed that chlorine concentrations (0.07–0.09 ppm) and methane concentrations (200–300 ppm) remained far below permissible exposure limits (0.5 ppm for Cl_2) and the methane alarm threshold of 5000 ppm, corresponding to 10% of the LEL, ensuring safe working conditions.

The results of this study imply the necessity of a transition from passive safety measures to proactive, intelligent sensing networks. The use of heterogeneous sensors—metal-oxide (MQ-4) for methane concentration trend monitoring and electrochemical (ZE03) for high-selectivity chlorine detection—indicates the importance of tailoring sensor materials to specific industrial hazards. Furthermore, the ESP32-S3 MCU enables local sensor-data acquisition and efficient transmission to the backend server, supporting low-latency safety monitoring. Although the current system utilizes cost-effective metal oxide sensors, advanced sensor technologies, such as platinum-decorated ZnO nanorods or $MoS_2/Ce_2Sn_2O_7$ heterojunctions, must be tested to enhance sensitivity and selectivity at room temperature. Further reduction in power consumption during continuous Wi-Fi/UWB transmission is required, and machine-learning methods should be integrated to minimize false positives during high-intensity work activities.

The developed safety helmet offers a robust, scalable solution for personnel protection, effectively mitigating the risks of physical accidents and biochemical hazards in the most challenging industrial environments. The integration of multi-sensor fusion localization, fall detection, environmental gas monitoring, and real-time backend visualization demonstrates that the proposed system can reliably operate in confined workspaces, providing a robust safety framework for industrial operations.

Acknowledgments

This research was supported by the National Science and Technology Council of Taiwan (Project No.: NSTC 114-2622-E-992-005-).

References

1 M. Capelli-Schellpfeffer: IEEE Ind. Appl. Mag. **11** (2005) 36. https://doi.org/10.1109/MIA.2005.1380325
2 D. Zhang, L. T. Yang, M. Chen, S. Zhao, M. Guo, and Y. Zhang: IEEE Syst. J. **10** (2014) 1226. https://doi.org/10.1109/JSYST.2014.2346625
3 X. Shen, W. Cheng, and M. Lu: Tsinghua Sci. Technol. **13** (2008) 78. https://doi.org/10.1016/S1007-0214(08)70130-5

4 Y. Cao, C. Chen, D. St-Onge, and G. Beltrame: IEEE Internet Things J. **8** (2021) 13449. https://doi.org/10.1109/JIOT.2021.3066243
5 D. Janczak, W. Walendziuk, M. Sadowski, A. Zankiewicz, K. Konopko, M. Slowik, and M. Gulewicz: IEEE Access **12** (2024) 55843. http://dx.doi.org/10.1109/access.2024.3389986
6 P. Supanakoon and S. Promwong: J. Mob. Multimed. **17** (2021) 1. https://doi.org/10.13052/jmm1550-4646.17411
7 R. Jurdi, H. Chen, Y. Zhu, B. L. Ng, N. Dawar, and C. Zhang: IEEE Access **12** (2024) 41084. https://doi.org/10.1109/ACCESS.2024.3377237
8 Y. Wang, S. Sun, F. Miao, and Y. Xia: IEEE Access **13** (2025) 16683. https://doi.org/10.1109/ACCESS.2025.3532331
9 C. Hou, W. Liu, H. Tang, J. Cheng, X. Zhu, M. Chen, C. Gao, and G. Wei: Drones **8** (2024) 372. https://doi.org/10.3390/drones8080372
10 R. Ali, R. Liu, A. Nayyar, B. Qureshi, and Z. Cao: IEEE Access **9** (2021) 164206. https://doi.org/10.1109/ACCESS.2021.3132645
11 G. T. Lee, S. B. Seo, and W. S. Jeon: Proc. 2021 IEEE 18th Annual Consumer Communications and Networking Conf. (CCNC) (2021) 1. https://doi.org/10.1109/CCNC49032.2021.9369588
12 X. Li, J. Ye, Z. Zhang, L. Fei, W. Xia, and B. Wang: IEEE Sens. J. **24** (2024) 29219. https://doi.org/10.1109/JSEN.2024.3436864
13 K. Chaccour, R. Darazi, A. H. El Hassani, and E. Andrès: IEEE Sens. J. **17** (2017) 812. https://doi.org/10.1109/JSEN.2016.2628099
14 H. Chapman and Y. A. Owusu: IEEE Sensors J. **8** (2008) 203. https://doi.org/10.1109/JSEN.2007.913026
15 L. Aprilia, R. Nuryadi, A. G. Saputro, S. A. Wella, I. Md Isa, and S. Abu Bakar: IEEE Sensors J. **24** (2024) 29806. https://doi.org/10.1109/JSEN.2024.3445368
16 M. Ganesan, J. Li, and F. Wang: IEEE Sensors J. **26** (2026) 3597. https://doi.org/10.1109/JSEN.2025.3641160
17 J. C. Santamaria-Pedrón, R. Berkvens, I. Miralles, C. Reaño, and J. Torres-Sospedra: Electronics **15** (2026) 181. https://doi.org/10.3390/electronics15010181
18 I. Campero-Jurado, S. Márquez-Sánchez, J. Quintanar-Gómez, S. Rodríguez, and J. M. Corchado: Sensors **20** (2020) 6241. https://doi.org/10.3390/s20216241
19 T. Yu, S. Sun, Y. Zhao, L. Wang, P. Li, Z. Chen, X. Bi, and X. Shi: Water Reuse **12** (2022) 438. https://doi.org/10.2166/wrd.2022.156
20 C. Yang and Y. Liu: Appl. Sci. **16** (2026) 1034. https://doi.org/10.3390/app16021034
21 H. Yang, Y. Wang, S. Xu, J. Bi, H. Jia, and C. Seow: Sensors **24** (2024) 1703. https://doi.org/10.3390/s24051703
22 Z. Deng, H. Luo, X. Gao, and P. Liu: Appl. Sci. **15** (2025) 6501. https://doi.org/10.3390/app15126501
23 R. Nagpal, N. Ababii, and O. Lupan: Mater. Today Electron. **15** (2026) 100192. https://doi.org/10.1016/j.mtelec.2025.100192
24 S. Monica and F. Bergenti: Electronics **8** (2019) 334. https://doi.org/10.3390/electronics8030334
25 C.-L. Lin, W.-C. Chiu, T.-C. Chu, Y.-H. Ho, F.-H. Chen, C.-C. Hsu, P.-H. Hsieh, C.-H. Chen, C.-C.K. Lin, and P.-S. Sung: Sensors **20** (2020) 5774. https://doi.org/10.3390/s20205774
26 E. Garcia, P. Poudereux, A. Hernandez, J. Urena, and D. Gualda: Proc. 2015 IEEE Int. Conf. Industrial Technology (ICIT) (2015) 3386–3391. https://doi.org/10.1109/ICIT.2015.7125601
27 D. Zhao, T. Song, J. Gao, D. Li, and Y. Niu: IEEE Access **12** (2024) 26137. https://doi.org/10.1109/ACCESS.2024.3362958
28 C. Taramasco, M. Pineiro, P. Ormeño-Arriagada, D. Robles, and D. Araya: PeerJ **13** (2025) e19004. https://doi.org/10.7717/peerj.19004
29 J. B. Forsyth, T. L. Martin, D. Young-Corbett, and E. Dorsa: IEEE Trans. Autom. Sci. Eng. **9** (2012) 505. https://doi.org/10.1109/TASE.2012.2197390
30 A. H. Anwer, M. Saadaoui, A. T. Mohamed, N. Ahmad, and A. Benamor: Chem. Eng. J. **502** (2024) 157899. https://doi.org/10.1016/j.cej.2024.157899
31 X. Yuan, C. Li, X. Yin, Y. Yang, B. Ji, Y. Niu, and L. Ren: Biosensors **13** (2023) 313. https://doi.org/10.3390/